International Journal of Multiphase Flow 35 (2009) 661–675

Contents lists available at ScienceDirect

International Journal of Multiphase Flow

journal homepage: www.elsevier.com/locate/ijmulflow

A two-fluid model of gas-assisted atomization including flow through the nozzle, phase inversion, and spray dispersion

K. Pougatch [a], M. Salcudean [a,*], E. Chan [b], B. Knapper [b]

[a] Department of Mechanical Engineering, University of British Columbia, 2054-6250 Applied Science Lane, Vancouver, BC, Canada V6T 1Z4
[b] Syncrude Canada Ltd,, Edmonton Research Centre, 9421 17th Avenue, Edmonton, AB, Canada T6N 1H4

ARTICLE INFO

Article history:
Received 23 June 2008
Received in revised form 17 February 2009
Accepted 9 March 2009
Available online 19 March 2009

Keywords:
Numerical modelling
Particle number density
Phase inversion
Turbulence

ABSTRACT

This paper describes a new approach to modelling compressible gas–liquid flows that undergo change of the continuous phase. The presented model includes the system of the ensemble averaged Navier–Stokes equations together with the particle number density equation for each phase. The constitutive equations that depend on the flow regime are obtained from many sub-models that have been developed alongside the main model. Droplet size is allowed to vary in the flow field but is considered constant within a control volume. Bubbles and droplets break-up and coalescence models are adapted to the flow conditions. The proposed model for atomization treats it as a catastrophic phase inversion that takes place over the surface determined by the local values of phase volume fractions. The model is applied to simulate the premixed air-assisted atomization of water in a nozzle-type device. The computational domain includes the nozzle and the surrounding area of the spray dispersion. The model performance has been verified by comparing the predicted and measured liquid flow rates in the spray as well as the pressure values along the nozzle wall. Computational results are analysed, and the main flow features are presented.

1. Introduction

Liquid sprays are widely used in various industrial applications where either the increase of the surface area of the liquid is desired, or some other properties of spray, for example, the droplet size distribution, the spraying angle and pattern, play a critical role in the process. There are two major types of the atomization devices: pressure jets and two-fluid atomizers (Nasr et al., 2002). The pressure jet is basically a pipe with an orifice at the end, through which the liquid is pushed, while the two-fluid atomizers bring gas and liquid together in a more sophisticated nozzle design. The two-fluid atomizers are also called gas-assisted because of an additional shear created by the gas injection. Depending on where gas and liquid come into contact, two-fluid atomizers can be internal or external: in the internal atomization gas is injected someplace upstream of the nozzle orifice and in external – downstream. It is known that gas-assisted atomization produces more finely dispersed droplets (Nasr et al., 2002). One of the various designs of the internal atomization device employs the continuous phase inversion, which is the change of the continuous phase from liquid to gas, as a primary method of obtaining liquid droplets. In this device the compressed gas is injected into the liquid, then the mixture travels through the variable cross-section nozzle; near the nozzle exit the gas rapidly expands causing catastrophic phase inversion and, thus, forming the droplets. There are a number of processes that take place simultaneously or sequentially during the operation of the described atomizer, such as compressible gas–liquid flow through the nozzle at high gas volume fraction, bubbles coalescence and break-up, phase inversion and primary droplets formation, droplets dispersion, and secondary droplets break-up and coalescence.

In order to simplify modelling, the sprays are often decoupled from the atomizer, so that only the spray dispersion is modelled. Such models usually employ the Lagrangian description of the droplets movement, i.e. direct tracking of each droplet, as the concentration of the dispersed phase is relatively small and the description of the droplets properties is significantly easier. One of the first such models was proposed by Dukowicz (1980). Even though the original model did not consider secondary break-up, coalescence, and size variations of droplets, it can be generalized to include these phenomena, e.g. Shi and Kleinstreuer (2007). The Eulerian description of the spray as a continuum is also possible, but it is not very popular in the spray-only computations. There are also attempts to improve the Eulerian scheme by building up on its advantages in predicting the chaotic motion of the particles. Beck and Watkins (2003) proposed a model that utilizes moments of the droplet distribution function making the computations more efficient. Nijdam et al. (2006) considered both the Lagrangian and Eulerian approaches and confirmed that the results

* Corresponding author. Tel.: +1 604 822 2732; fax: +1 604 822 2403.
E-mail address: msal@interchange.ubc.ca (M. Salcudean).

0301-9322/$ - see front matter © 2009 Elsevier Ltd. All rights reserved.
doi:10.1016/j.ijmultiphaseflow.2009.03.001

they produced are similar, provided the same sub-models are used; however, the ease of the implementation and a wider range of applicability make the Lagrangian method a preferred choice.

All separate spray models require the inlet boundary conditions to determine the initial droplet size distribution, the mass and momentum flux distributions, etc. While in some situations these values can be estimated or measured with sufficient accuracy, more often they are not well known. This makes necessary the inclusion of the atomization (or primary break-up) region into the modelling domain. The high liquid volume fractions in those regions make the Lagrangian approach not applicable. Vallet et al. (2001) proposed a simplified model for liquid jet atomization. They assumed that the large scale features of the flow, such as velocity, depend on the density ratio only, while the small scale features, such as droplet diameter, depend on the surface tension and turbulence. In addition, a single phase momentum equation with a variable density is used to represent the flow motion following the Eulerian approach. This model was applied to predict the droplets flow rates and the mean droplet diameter distribution throughout the spray area.

Von Berg et al. (2005) developed the first coupled model that includes the nozzle and the spray regions. The authors demonstrated two coupling approaches: first, the sequential applications of the nozzle flow model, primary break-up model, and discrete droplet model; and second, the fully coupled approach, where the multi-fluid (Eulerian) model equations are applied to the whole domain with different interfacial exchange terms. Even though the description of the break-up rate was significantly simplified in the second approach, the authors concluded that it has a better potential than the first one due to better resolution of the flow features.

Another coupled spray atomization model of Deux and Sommerfeld (2006) divides the computational domain in dense and dilute spray regions. In the dense region the two-fluid model is applied together with the atomization model based on the structure formation process, and in the dilute region the Lagrangian droplet tracking is employed. A good agreement with experimental data was reported, but still more work is required on the treatment of the boundary between the two regions.

The existing models consider the liquid jet break-up as a mechanism for the primary atomization. However, in the case of the premixed atomization under consideration, it is the phase inversion that is responsible for this process. Even though the phase inversion has been studied by many researchers, e.g. Vaessen et al. (1996), to the best of our knowledge the phase inversion theory has not been previously applied to the premixed atomizers.

In the existing coupled nozzle spraying models the flow through the nozzle itself is fairly straightforward, even though it might be complicated by cavitation, as it is the case for von Berg et al. (2005). However, in the gas-assisted premixed atomization the solution for the compressible high gas volume fraction flow is non-trivial. Recently, Pougatch et al. (2008) developed the two-fluid gas-compressible model for the nozzle flow. The model assumes a monodispersed distribution of the bubbles that is determined by solving a particle number density equation including break-up and coalescence terms. The mixture turbulence model adapted from Behzadi et al. (2004) with modified wall functions was used to close the system of equations. A new sub-model was proposed for the virtual mass forces at the high gas volume fractions. The model results compared well with the experimentally measured pressure variation along the nozzle wall and with the average value of the bubble diameter inside the nozzle.

In the present paper a fully coupled two-fluid model that includes gas–liquid flow inside and outside of the nozzle is presented. This model is based on the nozzle flow model developed previously by Pougatch et al. (2008). A single set of the flow and turbulence equations is solved throughout the whole modelling domain; however, some closure relationships are different depending on which of the phases is continuous in the flow region. This unified approach enables efficient numerical application of the model. Both the interfacial drag and turbulence induced break-up mechanisms are considered for gas bubbles and liquid particles. A simple sub-model of the catastrophic phase inversion is incorporated into the model to simulate the change of the flow regime from the churn-turbulent flow in the nozzle to the droplet dispersed flow in the spray. All of the closure relationships are taken from the published literature without any adjustments. The model numerical application is discussed and the results are analysed. The predictions of the pressure in the nozzle and the liquid mass flow rate in the spray at different distances from the nozzle orifice are compared with experimental results.

2. Model description

An Eulerian multi-fluid description is adopted for both continuous and dispersed phases. The advantage of this approach is that it can be applied to any flow region regardless of the local values of the volume fraction. It is assumed that both phases are interpenetrating; either the gas bubbles are dispersed in the liquid or the liquid droplets are dispersed in the gas. In order to reflect variation in particulate size and, at the same time, keep the solution economical, particle size distribution is considered locally monodispersed. That means that size variations are permitted throughout the flow field, but only one average diameter is used to represent particle sizes within a control volume. The gaseous phase is compressible, while the liquid is not. There is no mass or heat transfer between the phases; the gas flow is assumed to be adiabatic.

2.1. Mass, momentum and energy balance

The conservation equations for the model are obtained with ensemble averaging of the Navier–Stokes equations (Drew and Passman, 1999; Zhang and Prosperetti, 1994). Only the final forms are presented here, where all the variables are already averaged, unless noted otherwise. For convenience of presentation and for ease of implementation into the computer code, the equations are written in a phase independent way whenever possible. Because the model will be applied to the curvilinear geometry, a coordinate independent form is used. Continuous and disperse phases are denoted by $i = c, d$ with the densities ρ_i, the volume fractions α_i, and the velocities $\mathbf{V}_i$. Depending on the locally continuous phase, the subscript "i" can indicate "g" – gas, or "l" – liquid. The mass balance equation takes the following form:

$$\frac{\partial}{\partial t}\alpha_i\rho_i + \nabla\cdot\alpha_i\rho_i\mathbf{V}_i = 0. \tag{1}$$

Similarly, the momentum conservation can be written as

$$\frac{\partial}{\partial t}\alpha_i\rho_i\mathbf{V}_i + \nabla\cdot\alpha_i\rho_i\mathbf{V}_i\mathbf{V}_i = \nabla\cdot\boldsymbol{\tau}_i - \alpha_i\nabla P_i + \rho_i\mathbf{g} + \mathbf{F}_i^{drag} + \mathbf{F}_i^{turb} + \mathbf{F}_i^{vm}, \tag{2}$$

where $\boldsymbol{\tau}_i$ are the combined shear stresses, P_i – the phase pressures, $\mathbf{g}$ – the gravitational acceleration, and $\mathbf{F}_i$ – the interfacial (drag, turbulent drag, and virtual mass) forces. The shear stresses for the continuous phase contain the viscous and the turbulent (Reynolds) parts, while for the dispersed phase only the turbulent stresses are present.

$$\boldsymbol{\tau}_i = \delta_{ic}\boldsymbol{\tau}_i^{\mu} + \boldsymbol{\tau}_i^{t}, \tag{3}$$

where δ_{km} is the Kronecker symbol, which equals unity when indexes are the same, and zero – otherwise. The viscous stress tensor is defined as

$$\tau_c^{\mu} = \alpha_c \mu_c \left(\left(\nabla \mathbf{V}_c + \nabla \mathbf{V}_c^T \right) - \frac{2}{3} \mathbf{I} \nabla \mathbf{V}_c \right), \tag{4}$$

where μ_c is the molecular viscosity. The Boussinesq approximation in the form analogous to single phase flows is employed to calculate turbulent stresses:

$$\tau_i^t = \alpha_i \mu_i^t \left(\left(\nabla \mathbf{V}_i + \nabla \mathbf{V}_i^T \right) - \frac{2}{3} \mathbf{I} \nabla \mathbf{V}_i \right) - \frac{2}{3} \alpha_i \rho_i k_i \mathbf{I}, \tag{5}$$

where μ_i^t is the turbulent viscosity, k_i – the turbulence kinetic energy, and $\mathbf{I}$ is the unit tensor. For the gas with the temperature T_g and the specific heat c_{p_g}, the total enthalpy H_g is defined as

$$H_g = c_{p_g} T_g + \frac{\mathbf{V}_g^2}{2} + k_g \rightarrow \text{const}. \tag{6}$$

Instead of solving a full energy equation, a constant total enthalpy is assumed because of the adiabatic nature of the process and negligibly small viscous heat dissipation. In order to connect the gas density with the pressure, an ideal gas equation of state is applied.

$$P_g = \frac{\rho_g R T_g}{M_g}, \tag{7}$$

where M_g is the molar mass, and R is the universal gas constant.

The above balance equations alone do not provide sufficient description of the flow. Additional closure relationships need to be developed in order to provide missing links between micro scale physical phenomena and macro scale variables. This development is presented in subsequent sections.

2.2. Interfacial and boundary conditions

At the interface between gaseous and liquid phases the normal stresses are balanced

$$\left(-P_d + \tau_d^n\right) - \left(-P_c + \tau_c^n\right) = \frac{4\sigma}{d}. \tag{8}$$

A no-slip condition is used along the nozzle wall. The wall functions, which were modified for two-phase flow by Pougatch et al. (2008), are used to determine the values for the turbulent kinetic energy and its dissipation near the wall. The values in the cell centre adjacent to the wall are:

$$k = \frac{\xi^2}{\sqrt{C_\mu}}, \tag{9}$$

$$\varepsilon = \frac{\xi^3}{\kappa y}, \tag{10}$$

where κ is von Karman constant, calculated as:

$$\kappa^2 = \sigma_\varepsilon (C_{\varepsilon 2} - C_{\varepsilon 1}) \sqrt{C_\mu}, \tag{11}$$

and ξ is the averaged tangential velocity near the wall:

$$\xi = \sqrt[4]{\frac{\sum_i \alpha_i \rho_i U_{i\tau}^4}{\sum_i \alpha_i \rho_i}}, \tag{12}$$

where $U_{i\tau}$ is the phase tangential velocity near the wall.

The shear stress at the wall τ_{iw} for each phase is calculated as:

$$\tau_{iw} = U_{i\tau}^2 \rho_i \alpha_i, \tag{13}$$

where i is the phase index.

At the inlet constant mass flow rates are assumed for gas and liquid. The inlet pressure, velocities, and volume fractions are found as part of the solution.

Along the boundary separating the open part of the modelling domain from the ambient gas an equal pressure conditions is assumed. Gas can enter or exit the computational domain depending on the local conditions.

2.3. Interfacial forces

Only the drag, turbulent drag, and the virtual mass forces are considered in the model. The drag force accounts for the friction resulting from the difference of mean phase velocities. It is proportional to the difference of the mean phase velocities (Drew and Passman, 1999).

$$\mathbf{F}_d^{drag} = \frac{3}{4} \frac{\alpha_d \rho_c C_D^d}{d} |\mathbf{V}_c - \mathbf{V}_d| (\mathbf{V}_c - \mathbf{V}_d); \quad \mathbf{F}_c^{drag} = -\mathbf{F}_d^{drag}, \tag{14}$$

where d is the particle (bubble or droplet) diameter. The drag coefficient C_D^d depends on the flow regime. According to the existing flow regime maps, e.g. Taitel and Dukler (1976), flow in the pipe leading to the nozzle is in the dispersed bubble or churn-turbulent flow regime. We assume that the same flow regime persists through the length of nozzle. Therefore, the Ishii and Zuber (1979) correlation can be applied for the drag coefficient of the deformed gas bubbles.

$$C_D^g = \frac{8}{3} (1 - \alpha_d)^2. \tag{15}$$

After the atomization, the flow is in the dispersed bubbles flow regime. When the gaseous phase is continuous, the widely used model of Schiller and Naumann (1935) is employed:

$$C_D^l = \begin{cases} \frac{24(1+0.15\mathrm{Re}^{0.687})}{\mathrm{Re}} & \mathrm{Re} \leqslant 1000, \\ 0.44 & \mathrm{Re} > 1000, \end{cases} \tag{16}$$

where Re is the droplet Reynolds number, which is calculated as

$$\mathrm{Re} = \frac{\rho_c |\mathbf{V}_c - \mathbf{V}_d| d}{\mu_c}. \tag{17}$$

To calculate the turbulent drag force, we utilize the model of Viollet and Simonin (1994).

$$\mathbf{F}_d^{turb.drag} = \frac{3}{4} \frac{\alpha_c \alpha_k \rho_c C_D}{d_k} |\mathbf{V}_c - \mathbf{V}_d| \mathbf{V}_{drift}; \quad \mathbf{F}_c^{turb.drag} = -\mathbf{F}_d^{turb.drag}, \tag{18}$$

where $\mathbf{V}_{drift}$ is the drift velocity, calculated as

$$\mathbf{V}_{drift} = \frac{\mu_m^t}{\rho_m Sc^t} \left(\frac{\nabla(\rho_c \alpha_c)}{\rho_c \alpha_c} - \frac{\nabla(\rho_d \alpha_d)}{\rho_d \alpha_d} \right). \tag{19}$$

The turbulent Schmidt number Sc^t in this equation is assumed 0.7.

The virtual mass force appears due to the acceleration of the continuous phase that is carried away together with the accelerating discrete particle. It is defined in a following way (Drew and Passman, 1999):

$$\mathbf{F}_d^{vm} = C_{vm} \alpha_d \rho_c \left[\left(\frac{\partial \mathbf{V}_c}{\partial t} + \mathbf{V}_c \cdot \nabla \mathbf{V}_c \right) - \left(\frac{\partial \mathbf{V}_d}{\partial t} + \mathbf{V}_d \cdot \nabla \mathbf{V}_d \right) \right];$$
$$\mathbf{F}_c^{vm} = -\mathbf{F}_d^{vm}. \tag{20}$$

The virtual mass coefficient C_{vm} depends on the volume fraction of the dispersed phase. Pougatch et al. (2008) modification of Laurien and Niemann (2004) polynomial correlation is adopted for use with the model.

$$C_{vm} = \min \left\{ 0.5 + 1.63\alpha_d + 3.85\alpha_d^2; \ \frac{\alpha_c}{\alpha_d} \right\}. \tag{21}$$

The lift force is neglected in the model because in the region of the liquid-continuous flow the disperse phase volume fractions are very high and the lift coefficient is negligibly small, according to the Behzadi et al. (2004) correlation, and in the gas-continuous flow the lift force is insignificant due to the high density ratio. Other forces, such as the wall lubrication force, the Faxén force, and the Basset force are also ignored.

2.4. Turbulence modelling

2.4.1. Mixture turbulence model

The fluctuating motion of the phases plays an extremely important role in determining the microscopic structures in the two-phase flow. These structures influence the break-up and coalescence processes as well as momentum dissipation through the Reynolds stresses, which, in turn, have a significant influence on the macroscopic flow parameters. Thus, it is crucial for the success of the simulations to have a turbulence model that accurately represents the complex nature of the process. The widely used single phase k–ε model can be extended to multiphase flows. Kataoka and Serizawa (1989) obtained the equations for the turbulent kinetic energy (k) and its dissipation rate (ε) for each phase using the same approach as for the single phase equations. However, the well known problem of finding appropriate closures for the equations due to the inability to model some terms becomes even more difficult for multiphase flow turbulence. The equations need to be substantially simplified for practical use. The mixture turbulence model approach proposed by Gosman et al. (1992) and further developed by Behzadi et al. (2004) was chosen. In this approach, the turbulence kinetic energy and its dissipation rate equations for both phases are added, and the final equations are written in terms of the mixture variables. This is made possible due to an assumption that the velocity fluctuations in the dispersed phase are directly proportional to the velocity fluctuations in the continuous phase:

$$\mathbf{v}'_d = C_t \mathbf{v}'_c, \tag{22}$$

where C_t is turbulence response coefficient, which depends on the flow parameters. It follows from Eq. (13) that the turbulence kinetic energy and the dissipation rate are also directly proportional:

$$k_d = C_t^2 k_c, \tag{23}$$

$$\varepsilon_d = C_t^2 \varepsilon_c. \tag{24}$$

The resulting equations take the following form:

$$\frac{\partial}{\partial t}(\rho_m k) + \nabla \cdot (\rho_m \mathbf{V}_m k) = \nabla \cdot \frac{\mu_m}{\sigma_k} \nabla k + Q - \rho_m \varepsilon + S, \tag{25}$$

$$\frac{\partial}{\partial t}(\rho_m \varepsilon) + \nabla \cdot (\rho_m \mathbf{V}_m \varepsilon) = \nabla \cdot \frac{\mu_m}{\sigma_\varepsilon} \nabla \varepsilon + \frac{\varepsilon}{k}(C_{\varepsilon 1} Q - C_{\varepsilon 2} \rho_m \varepsilon + C_{\varepsilon 3} S). \tag{26}$$

In the above equations $\sigma_k = 1.0$, $\sigma_\varepsilon = 1.3$, $C_{\varepsilon 1} = 1.44$, $C_{\varepsilon 2} = 1.92$ are standard values for the model closure coefficients, Q is the turbulence production due to shear, and S is the turbulence production/sink due to interfacial interactions. An additional coefficient, $C_{\varepsilon 3}$, specific to the multiphase flow is assumed 1.2, according to Simonin and He (1992).

Knowing values of k and ε for each phase, the turbulent viscosities used in Eq. (5) can be calculated in the usual way:

$$\mu_i^t = C_\mu \rho_i \frac{k_i^2}{\varepsilon_i}, \tag{27}$$

where $C_\mu = 0.09$ is the coefficient from the standard k–ε model. The weighted mixture properties, used in Eqs. (16) and (17), are calculated as follows (Behzadi et al., 2004):

$$\rho_m = \sum_i \alpha_i \rho_i, \tag{28}$$

$$k_m = \frac{\sum_i \alpha_i \rho_i k_i}{\rho_m}, \tag{29}$$

$$\varepsilon_m = \frac{\sum_i \alpha_i \rho_i \varepsilon_i}{\rho_m}, \tag{30}$$

$$\mu_m = \frac{\left(\alpha_c \mu_c + \alpha_d \mu_d C_t^2\right)\rho_m}{\alpha_c \rho_c + \alpha_d \rho_d C_t^2}, \tag{31}$$

$$\mathbf{V}_m = \frac{\alpha_c \rho_c \mathbf{V}_c + \alpha_d \rho_d \mathbf{V}_d C_t^2}{\alpha_c \rho_c + \alpha_d \rho_d C_t^2}. \tag{32}$$

The production of turbulence due to the flow shear is obtained as a sum of each phase production terms:

$$Q = \sum_i (\boldsymbol{\tau}_i^t \cdot \nabla \mathbf{V}_i). \tag{33}$$

The additional production term S consists of two parts. First part, S_1, is the turbulence dissipation by the dispersed phase, and the second, S_2, is the so-called bubble/droplet induced turbulence. In order to find S_1, the interfacial force terms in the instantaneous phase momentum balance equation are multiplied by the fluctuating velocity of the corresponding phase and averaged. This way the drag induced dissipation is obtained:

$$S_1^{drag} = -2\gamma k_c (C_t - 1)^2, \tag{34}$$

where γ is the friction coefficient, defined as:

$$\gamma = \frac{3}{4} \frac{\alpha_d \rho_c C_D^d}{d} |\mathbf{V}_c - \mathbf{V}_d|, \quad \text{see Eq. (14)}. \tag{35}$$

Similarly, the virtual mass induced dissipation can also be obtained. It can be written as

$$S_1^{vm} = \alpha_d \rho_c (C_t - 1) F(\mathbf{V}_c, \mathbf{V}_d), \tag{36}$$

where F is a function, which depends on the phase velocity. The exact expression for this function is quite lengthy, and for the sake of brevity is not presented. Also, it will be shown in the discussion below that this function is not required in the model. The bubble or droplet induced turbulence S_2 is calculated following Troshko and Hassan (2001), who using the results of Kataoka and Serizawa (1989) demonstrated that

$$S_2 = \left(\mathbf{F}_d^{drag} + \mathbf{F}_d^{turb} + \mathbf{F}_d^{vm}\right) \cdot (\mathbf{V}_d - \mathbf{V}_c). \tag{37}$$

2.4.2. Turbulence response coefficient

The response coefficient defined in Eq. (13) depends on the flow regime. It was reported by Behzadi et al. (2004) that for the bubble volume fractions above 6%, the bubbles and the surrounding liquid have the same values of the fluctuating velocities; that means that the value of the response coefficient is unity. Inside the nozzle, where the liquid phase is continuous, the volume fraction of the discrete phase is expected to be much higher than 6%; therefore, the unity value of the response coefficient for the bubbles can be adopted.

In the flow areas where the gaseous phase is continuous (dispersed droplets flow regime) the Viollet and Simonin (1994) model is applied to determine the turbulence response coefficient. The model is based on the analysis of time scales for the turbulence in the dispersed phase. The response coefficient is calculated in the following way:

$$C_t = \sqrt{\frac{\tau_{cd}^t}{\tau_{cd}^F + \tau_{cd}^t}}. \tag{38}$$

The eddy-droplet interaction time, τ_{cd}^t is obtained from

$$\tau_{cd}^t = \frac{\tau_c^t}{\sqrt{1 + C_\beta \xi^2}}, \tag{39}$$

where τ_c^t is the time scale of the energetic turbulent eddies is

$$\tau_c^t = \frac{3}{2} C_\mu \frac{k_c}{\varepsilon_c}, \tag{40}$$

and the parameter ξ is given by

$$\xi = \frac{|\mathbf{V}_c - \mathbf{V}_d|}{\sqrt{\frac{2}{3}k_c}}. \tag{41}$$

Comparison with the experimental results of Wells and Stock (1983) leaded Viollet and Simonin (1994) to find that the coefficient C_β depends on the angle between the velocity of the particulate phase and the relative velocity: when they are parallel $C_\beta = 1.8$, and when they are perpendicular $C_\beta = 0.45$. Therefore, it can be written as a continuous function:

$$C_\beta = 1.8 - 1.35\left(\frac{\mathbf{V}_d \cdot (\mathbf{V}_c - \mathbf{V}_d)}{|\mathbf{V}_d||\mathbf{V}_c - \mathbf{V}_d|}\right)^2. \tag{42}$$

Finally, the characteristic time of particle entrainment by the fluid motion, τ_{cd}^F, is calculated as

$$\tau_{cd}^F = \frac{4}{3}\frac{\rho_d}{\rho_c}\frac{d}{C_D|\mathbf{V}_c - \mathbf{V}_d|}. \tag{43}$$

2.5. Particle number density

The dispersed phase, bubbles or droplets, consists of different size particles. They can undergo break-up or coalescence under certain conditions. There are a number of approaches to represent a variety of particle sizes in the two-phase flow. In this model the assumption of monodispersed particles is made. This way an average particle diameter represents the actual particles within each control volume. The average diameter can change from one point in the flow field to another. To describe its variation, we introduce the particle number density n, which is the number of particles in the unit volume defined as

$$n = \frac{6\alpha_d}{\pi d^3}. \tag{44}$$

The conservation equation for the particle number density was derived by Kolev (2002a).

$$\frac{\partial n}{\partial t} + \nabla \cdot (\mathbf{V}_d n) = \nabla \cdot \left(\frac{\mu_d^t}{\rho_d Sc^t}\nabla n\right) + n(f_{br} - f_{coal}). \tag{45}$$

It is a convection–diffusion transport equation with the source and sink terms on the right hand side that are described by means of the frequencies of break-up, f_{br}, and coalescence, f_{coal}. Note that the break-up frequency is defined for a single particle (bubble or droplet). In order to solve this equation, it is necessary to find appropriate models for these frequencies. As there are two distinct flow regimes under consideration, bubbles in liquid and droplets in gas, each of them needs to be analysed separately.

2.5.1. Bubbles break-up and coalescence

Most of the models for bubbles break-up and coalescence were developed either for individual bubbles or for bubble column reactors. The conditions, generally encountered in such systems, are different from the compressible flow in the nozzle in terms of the lower values of gas volume fraction and lower flow rates. However, the extrapolation of the existing models with some corrections done by Pougatch et al. (2008) produced plausible results that agreed well with experimental observations. The same approach is used in the current study.

Bubble stability is determined by the ratio between the shear forces and the surface tension forces. The shear forces can arise due to the fluctuating motion or to the interfacial drag. The Martinez-Bazan et al. (1999) break-up frequency relationship is used

$$f_{br} = K\frac{\sqrt{(V^{rel})^2 - \frac{12\sigma}{\rho_c d}}}{d}, \tag{46}$$

where σ is the surface tension, V^{rel} – the relative velocity, and K – the constant to be determined experimentally. The authors suggested using the value 0.25. Depending on the dominant break-up mechanism, V^{rel} can be either the mean value of the turbulent velocity fluctuations, which is obtained using Kolmogorov's (1949) theory of turbulence, or the difference between the velocities of the continuous and discrete phase.

$$(V^{rel})^2 = \max\left\{\beta(\varepsilon d)^{\frac{2}{3}};\ (\mathbf{V}_c - \mathbf{V}_d)^2\right\}, \tag{47}$$

where $\beta = 8.2$ is the constant given by Batchelor (1956).

Coalescence frequency is the product of the collision frequency, f_{coll}, and coalescence probability, P_{coal}:

$$f_{coal} = f_{coll}P_{coal}. \tag{48}$$

The collision frequency relationship can be obtained considering the elastic collisions of hard spheres with uniform spatial distribution (see Kolev, 2002b) with the Hibiki and Ishii (1999) proposed modification to take into account the volume reduction due to the presence of the dispersed phase:

$$f_{coll} = \frac{3}{2}\frac{\alpha_d}{(\alpha_d^{\max} - \alpha_d)d}V^{rel}, \tag{49}$$

where $\alpha_d^{\max}$ is the maximum volume fraction of the dispersed phase (bubbles), before the flow regime changes due to the catastrophic phase inversion.

For the collision probability Chesters (1991) model is applied:

$$P_{coal} = \exp\left(-c\sqrt{0.5We_d}\right), \tag{50}$$

where We_d is the Weber number defined as:

$$We_d = \frac{\rho_c(\varepsilon d)^{\frac{2}{3}}d}{2\sigma}, \tag{51}$$

and $c = 0.4$ is the model constant.

2.5.2. Droplets break-up and coalescence

Similarly to the bubble break-up, the droplet break-up also depends on the balance between the surface stresses, determined by the surface tension σ, and the external stresses that can be different in nature. For the high speed jets, the dynamic forces associated with the relative motion of the droplet and with the fluctuating velocities around the droplet play the dominant role, as viscous effects are relatively small. In this case, the droplet Weber number can be introduced, as the ratio of the shear to surface tension forces:

$$We_d = \frac{\rho_c V^{rel} d}{\sigma}. \tag{52}$$

Kolmogorov (1949) and Hinze (1955) proposed a Weber number based droplet break-up model. It postulates that if the droplet Weber number is below the critical value, $We_d \leqslant We_{cr}$, the droplet is stable, and if it is above, $We_d > We_{cr}$, – the droplet will break-up. Thus, the maximum stable droplet diameter can be found from the critical Weber number:

$$d_{st} = \frac{We_{cr}\sigma}{\rho_c V^{rel}}. \tag{53}$$

Both of these researchers considered only the turbulence induced break-up. The same theory can be extended to the drag induced break-up as well, provided an appropriate value for the relative velocity V^{rel} is used. Kocamustafaogullari et al. (1994) showed that the critical Weber numbers are different depending on the break-up

mechanism considered. The researchers obtained the relationship, which connects both critical Weber numbers:

$$We_{cr}^{turb} = k_{We}\left(\frac{\rho_c}{\rho_d}\right)^{\frac{2}{3}}\frac{(\rho_d-\rho_c)}{\rho_d}We_{cr}^{drag}, \tag{54}$$

where k_{We} is the coefficient, which for the air-water flow at about atmospheric pressure is close to unity.

Let us first consider the drag induced break-up. In this case, the relative velocity is the absolute value of the difference between the average velocities of the phases:

$$V^{rel} = |\mathbf{V}_c - \mathbf{V}_d|. \tag{55}$$

It was found by Brauer (1992) and reported by Kolev (2002b) that the critical Weber number for the drag induced break-up is also Reynolds number dependent. If the droplet Reynolds number is defined as

$$Re_d = \frac{\rho_c|\mathbf{V}_c - \mathbf{V}_d|d}{\mu_c}, \tag{56}$$

then the dependency correlation takes the following form:

$$We_{cr}^{drag} = \begin{cases} 25, & \text{for } Re_d < 200, \\ 55\left(\frac{24}{Re_d} + \frac{20.1807}{Re_d^{0.615}} - \frac{16}{Re_d^{0.667}}\right), & \text{for } 200 \leqslant Re_d < 2000, \\ 5.48, & \text{for } Re_d \geqslant 2000. \end{cases} \tag{57}$$

The critical Weber number criterion determines whether the droplet will break-up or not; in addition, it is also required to know how the droplet will break-up. In contrast with the bubble break-up, where the bubble most often just splits into two daughter bubbles, there are several fragmentation modes for the droplet break-up. There are some variations between different authors regarding the classifications of the modes, e.g. Kolev (2002b), Lee and Reitz (2001), Shi and Kleinstreuer (2007); however, the general features of the break-up do not change. In this paper we will use Kolev (2002b) classification. The different break-up regimes are summarized in Table 1.

The vibration break-up is characterised by droplet oscillation with their natural frequency and its subsequent decomposition into two parts. The bag break-up happens when the droplet is deformed into the hollow semi-spherical shape, and then, when the wall becomes too thin, burst into droplets of various sizes. The bag and stamen break-up is the variation of the previous mode, the difference is that during the "bag" formation a column of liquid parallel to the flow is also formed along the axis of the droplet. This column will burst after the "bag". As the name implies, during the stripping break-up, small droplets are stripped from the surface of the original droplet. Finally, in the catastrophic break-up the droplet disintegrates into large fragments, which in turn, break further down instantly.

The time it takes for a droplet to break, the break-up time $\Delta\tau_{br}$, depends on the fragmentation mode. By analysing experimental data, Pilch et al. (1981) developed a correlation for the dimensionless break-up time, $\Delta\tau_{br}^*$, defined as

$$\Delta\tau_{br}^* = \Delta\tau_{br}\frac{|\mathbf{V}_c|}{d}\sqrt{\frac{\rho_c}{\rho_d}}. \tag{58}$$

This correlation connects the break-up time to the droplet Weber number in the following form:

$$\Delta\tau_{br}^* = c(We_d - 12)^m, \tag{59}$$

where the constants c and m are determined from Table 2 depending on the droplet Weber number.

Evidently, the break-up frequency depends on the break-up time and the fragmentation mode. In the vibration break-up, two new droplets are produced instead of one. Thus, the frequency can be calculated as

$$f_{br} = \frac{1}{\Delta\tau_{br}}, \quad We_d \leqslant 12. \tag{60}$$

For the bag, bag and stamen, and stripping break-ups the frequency will depend on the number of droplets produced. Unfortunately, the process is not investigated or understood well enough to provide a definite value of this number. Kolev (2002b) reported that it varies from 30 to 110, while Beck and Watkins (2003) assumed the value of 8 for their model. In the presented model a general approach proposed by Kolev (2002b) is used that does not employ the number of daughter droplets directly. (However, this number can be easily deduced from the model.) The break-up frequency is obtained from the stable droplet diameter (Eq. (53)), current droplet diameter, and the break-up time:

$$f_{br} = \frac{\left(\left(\frac{d}{d_{st}}\right)^3 - 1\right)}{\Delta\tau_{br}}. \tag{61}$$

In addition, to prevent the frequency from reaching unreasonably high values, the maximum number of daughter droplets is limited to 101. Thus, the maximum frequency $f_{br}^{\max}$ is calculated as:

$$f_{br}^{\max} = \frac{100}{\Delta\tau_{br}}. \tag{62}$$

On the other hand, the number of the resulting droplets cannot be less than two. So, the minimum frequency $f_{br}^{\min}$ can also be obtained.

$$f_{br}^{\min} = \frac{1}{\Delta\tau_{br}}. \tag{63}$$

Therefore, the following procedure is adopted. If the value obtained in Eq. (61) exceeds the maximum calculated by Eq. (62) or drops below the minimum calculated by Eq. (63), the maximum or minimum values respectively are used in the model. Similar ideas are used to predict the catastrophic break-up frequency. However, no limiting maximum value is used is this case as the number of daughter bubbles can be very large.

In the turbulent break-up the relative velocity is connected to the variation of the fluctuating velocity around the droplet. Using Kolmogorov (1949) theory, the velocity change over the distance d is

$$V^{rel} = C(\varepsilon_c d)^{\frac{1}{3}}, \tag{64}$$

Table 1
Droplet fragmentation modes classification.

Weber number	Fragmentation mode
$We_d \leqslant 12$	Vibration break-up
$12 < We_d \leqslant 18$	Bag break-up
$18 < We_d \leqslant 45$	Bag and stamen break-up
$5 < We_d \leqslant 350$	Stripping break-up
$We_d > 350$	Catastrophic break-up

Table 2
Constants in Eq. (59).

C	M	Weber number
7	0	$We_d \leqslant 12$
6	−0.25	$12 < We_d \leqslant 18$
2.45	0.25	$18 < We_d \leqslant 45$
14.1	−0.25	$45 < We_d \leqslant 50$
0.766	0.25	$350 < We_d \leqslant 2670$
5.5	0	$We_d > 2670$

where C is the constant of order one to be defined by experiments. In the present model it is assumed that $C = 1$. Substituting V^{rel} in Eq. (53), one can obtain the relationship for the stable droplet diameter:

$$d_{st} = \varepsilon_c^{-0.4}\left(\frac{We_{cr}^{turb}\sigma}{\rho_c}\right)^{0.6}. \tag{65}$$

The time needed for a break-up is estimated according to Kolev (2002b)

$$\Delta\tau_{br}^{t} = \left(\frac{d^2}{\varepsilon_d}\right)^{\frac{1}{3}}. \tag{66}$$

In order to find the break-up frequency, f_{br}^{turb}, Eqs. (61)–(63) are used with the stable droplet diameter from Eq. (65) and the break-up time from Eq. (66).

Finally, knowing the frequencies for the interfacial drag and turbulence induced break-ups, the largest one is assumed to determine the dominant mechanism under the particular flow conditions:

$$f_{br} = \max\{f_{br}^{drag};\ f_{br}^{turb}\}, \tag{67}$$

and this frequency value is used in Eq. (45).

The droplets coalescence probability, which is necessary to determine the coalescence frequency, is obtained with Lasheras et al. (1998) model:

$$P_{coal} = \exp\left(-\frac{T}{t}\right), \tag{68}$$

where T is the critical drainage time, and t – the droplet contact time, which are calculated as follows:

$$T = \frac{\mu_c}{\rho_d(\varepsilon_d d)^{\frac{2}{3}}}, \tag{69}$$

$$t = \frac{d^{\frac{2}{3}}}{\varepsilon^{\frac{1}{3}}}. \tag{70}$$

The collision frequency for the droplets is found in a similar way as for the bubbles (see Eq. (49)); however, no correction for the high loading of the particulate phase is needed, as the droplet volume fraction is generally low. Also, it needs to be noted, that the relative velocity required for the collision frequency depends on the fluctuating motion of the dispersed phase; hence, the dissipation value of the dispersed phase is used.

$$f_{coll} = \frac{3}{2}\frac{\alpha_d}{d}(\varepsilon_d d)^{\frac{1}{3}}. \tag{71}$$

The coalescence frequency is calculated from the collisions frequency and the coalescence probability by Eq. (48). Thus, Eq. (45) is closed for all flow regimes considered in the current model.

2.6. Atomization (phase inversion)

As the flow progresses through the nozzle, the gaseous phase expands and at a certain point, which can be located inside or outside the nozzle, the volume fraction of the liquid phase becomes too small to sustain the liquid-continuous flow regime and the gaseous phase assumes continuity. That is, the flow from the churn-turbulent/dispersed bubble flow regime transits to a dispersed droplet flow regime. This phenomenon is called the phase inversion. It can happen extremely fast, over a very thin surface, or there can be some transitional area where the parcels of various flow regimes are intertwined in time and space. Clearly, the interfacial interactions during the phase inversion are complex and not well understood; investigating those interactions would constitute by itself a very significant challenge to researchers in the future. Meanwhile, in order to make further progress with the model, it is necessary to introduce a number of assumptions that simplify the problem at the cost of loosing details in the representation of the phase inversion. First, we assume that the phase inversion takes place over an infinitely thin surface; such phase inversion is called catastrophic. While there is some work investigating the catastrophic phase inversion for emulsions, e.g. Vaessen et al. (1996) for the oil–water mixture, a comprehensive model for the gas–liquid flows is yet to be developed. Therefore, further assumptions are required. A simplified approach is proposed below, that allows the model to switch from one flow regime to another based on intuitive considerations. We assume that the location for the catastrophic phase inversion surface depends only on the local volume fraction values. If all the bubbles were round spheres of the same diameter, then the maximum volume fraction value for the ordered packing is well established and equals 0.74. However, in the high speed compressible flow in the nozzle, the bubbles can be deformed and, most importantly, their distribution is in reality polydispersed, which means that the gaps between the bigger bubbles can be filled with the smaller ones. Santiso and Muller (2002) investigated the packing of the polydispersed mixtures and concluded that the packing limit can reach values above 0.9. Wang et al. (2005) used the value of 0.8 to describe the transition from the churn-turbulent flow regime in the bubble column reactor. In addition, the experimental results of Deichsel and Winter (1990) suggest that for high speed critical flow in pipes, the transition from the churn-turbulent regime is delayed up to a volume fractions of 0.92. Evidently, there is a difference between the critical values of the volume fraction for a free shear flow and for a pipe flow. However, in the case under consideration, the transition happens in the immediate vicinity of the nozzle exit either upstream (in the nozzle) or downstream (outside the nozzle). Thus, it is more logical to use the pipe value for the description of the phase inversion. Also, an introduction of an additional unknown parameter would make the model application less convenient and create another non-trivial task of defining the extent of the influence of the nozzle wall boundaries downstream of the exit orifice. Therefore, it is assumed that the transition happens as soon as the local value of the gas volume fraction reaches $\alpha_d^{\max} = 0.8$ (80%). As the selection of this value is somewhat arbitrary (only the range is established), some additional studies are presented and discussed later in Section 3.5.

In order to determine the diameter of the newly formed droplets, it is assumed that the particle number density (or the number of particles) remains the same during the phase inversion. This assumption can be illustrated by a honeycomb structure where the cells represent the bubbles and the nodes represent the new droplets that will be formed when the bubbles simultaneously coalesce resulting in the catastrophic phase inversion. The increase of the surface area can be estimated as:

$$\frac{S_{droplet}}{S_{buble}} = \left(\frac{\alpha_d^{\max}}{1-\alpha_d^{\max}}\right)^{\frac{2}{3}}. \tag{72}$$

This is not a very large value compared with jet atomizers; therefore, the pressure drop across the phase inversion surface, associated with the energy loss due to the increase of the surface area can be ignored.

Other phase properties, such as the velocity and the turbulence parameters do not change as the flow passes through the phase inversion plane.

3. Model application

3.1. Numerical method

All of the main differential equations have been written independently of the nature of the locally continuous phase. Therefore,

each of them can be solved throughout the whole flow field without the explicit separation between the liquid-continuous and gas-continuous zones. The effects of the particular flow regime are accounted for by the closure equations. The developed solution method is described fully by Pougatch et al. (2008). It is based on Spalding (1980) IPSA procedure and involves curvilinear coordinate transformation for an accurate representation of the nozzle geometry. All interfacial terms, such as the drag and virtual mass forces, are implicitly accounted for during the solution of the momentum equations as well as during the pressure correction steps. Second order upwind discretization is used for all the equations, except the one for the volume fraction, for which a higher accuracy QUICK scheme (Leonard, 1979) is employed. This choice is necessary because of the high gradients of the droplet concentration near the periphery of the spray and the importance of this area for an accurate prediction of the spray shape. The GMRES matrix solver used in the calculations was obtained from the Netlib depository (SLATEC, 1993).

3.2. Experimental set up

The experimental part of this work has been conducted at the same spray test facilities at Syncrude Canada that were used to obtain the detailed pressure measurements along the nozzle wall by Pougatch et al. (2008). The nozzle, shown in the lower part of Fig. 1, is attached to the end of 1.25 m pipe that connects it to the mixing device where the compressed air is injected into the water. The whole assembly is schematically illustrated in the upper part of Fig. 1. The main focus of the described experiment was to obtain the water volume fluxes profiles across the jet at various distances. A probe, which was 1 cm (3/8 in.) diameter cylinder with one end open and another connected to a container that collected water, was placed in the spray to gather water at a certain position during a given amount of time. Knowing the water volume and time, an average flow rate can be calculated. By moving the probe from one position to another, the area of interest can be mapped. During the experiments, the cross-sectional profiles at distances 15.25 cm (6 in.) and 30.5 cm (12 in.) from the nozzle exit were obtained. In addition, the pressure was also measured at three points along the nozzle wall: after the mixer, before the nozzle, and right after the second convergent section of the nozzle. Two sets of the experimental conditions that represent two different gas to liquid mass ratios (GLR) were considered. The values of the flow rates of the air and water are presented in Table 3.

3.3. Computational domain

Axial symmetry is assumed for all simulated cases. For the flow inside the nozzle, the influence of the gravitational forces has been investigated by Pougatch et al. (2008) by modelling a three-dimensional case. They have concluded that the influence is small enough to be neglected. Let us consider the droplet moving outside of the nozzle. Assuming it has an average velocity of 50 m/s, its trajectory will deflect only about 2 mm after 1 m distance due to the action of the gravitational acceleration. Clearly, we can neglect gravity outside the nozzle as well. Therefore, the gravity term is omitted from the right hand side of Eq. (2). In addition, we assume that the nozzle is issuing in quiescent air. Thus, no wind influence is considered at this stage. With these assumptions all the flow equations and boundary conditions are axisymmetric; therefore, an axisymmetric simplification is warranted. As the model equations are written in terms of the generalized curvilinear coordinates, the actual shape of the computational domain will be a small angle wedge.

The modelling area starts right after the gas injection device. It includes the pipe leading to the nozzle, the nozzle itself, and the region of spray dispersion, which is about 80 cm long and has 20 cm

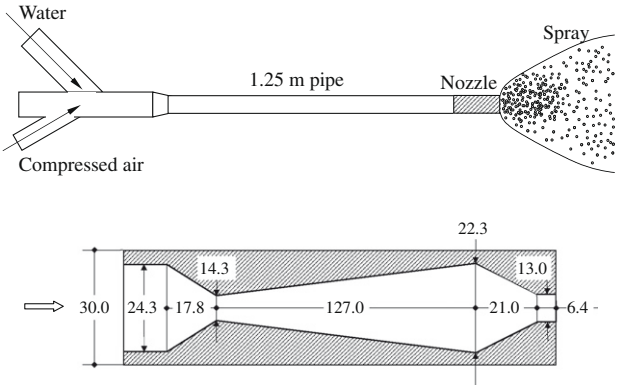

Fig. 1. Nozzle geometry (all dimensions are in mm; not to scale).

radius. The whole computational domain is shown in Fig. 2. Note, that the outside area does not start at the nozzle exit plane: it extents about 30 cm beyond it. The reason for this extension is to avoid having a boundary too close to the nozzle exit, where the gradients of pressure and velocity are still quite substantial.

The boundary conditions utilized in the simulations are also marked in Fig. 2. At the nozzle inlet, the air and water flow rates from Table 3 are assigned. The volume fraction is calculated based on the pressure, which is extrapolated from the inside of the domain during the solution. It was shown by Pougatch et al. (2008) that no matter what bubble diameter we chose at the inlet by the half length of the pipe it reaches the value determined by the balance between the break-up and coalescence processes. In this study the value of 10 mm is used. Nozzle walls, inside and outside, are treated according to the procedure described in Section 2.2. All outside boundaries are equal pressure boundaries, the pressure is atmospheric. If there is an inflow through these boundaries, then it is assumed that there are no droplets in the entering gas. The sides of the wedge are treated as symmetry boundaries, that is, no flux of any parameter can come through them.

It is shown in Fig. 3 that for the discretization, the computational domain was split in five segments. Note that only a small part of the entrance pipe is included in this figure. The mesh is highly non-uniform in order to provide a good resolution in the areas of high gradients, i.e. near the nozzle exit and around the edges of the spray. In order to assess grid independence, the solution for different grids needs to be evaluated. First of all, the grid independence of the solution of the flow inside the nozzle has already been investigated by Pougatch et al. (2008). Therefore, the current work focuses on the grid refinement outside of the nozzle in the spray area, leaving the nozzle grid the same. Three sets of numerical grid were considered: small (8524 grid cells), medium (11164 grid cells), and fine (15904 grid cells). The flow conditions, for which the grid independence study was conducted, correspond to Case 1 from Table 3. Even though the equations are transient and are solved in a fully transient mode, the final solution exhibits very limited time-dependence. Therefore, the converged results will be time-averaged and analysed as steady state. While there are some observable differences between the solutions on coarse and medium grids, the variations between the medium and fine

Table 3
Air and water flow rates for investigated cases.

Case #	1	2
Air flow rate (kg/s)	0.0442	0.0883
Water flow rate (kg/s)	2.2	2.2
GLR (%)	2	4

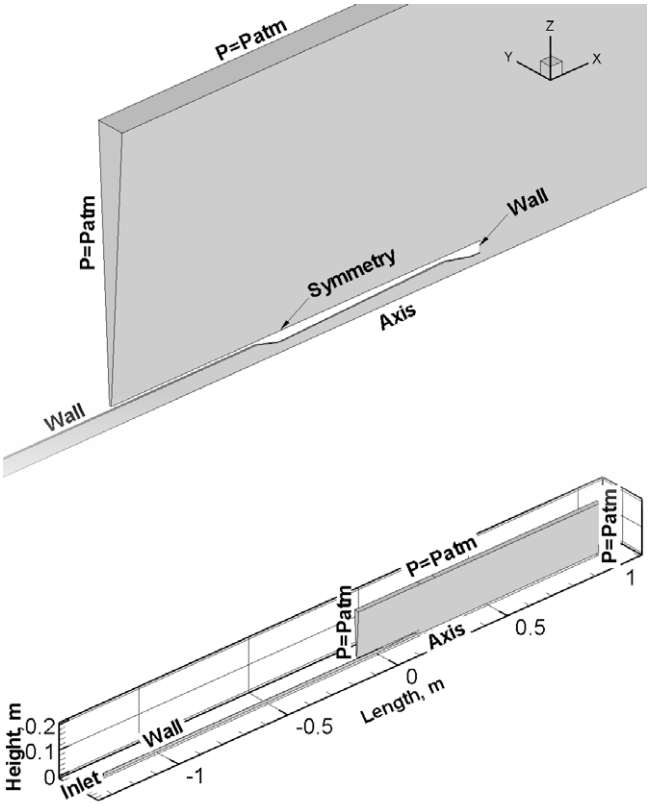

Fig. 2. Computational domain and boundary conditions (the area around the nozzle is magnified and shown in the upper part of the figure).

grid solutions are generally small. Thus, in all subsequent simulations presented in this paper, the medium grid is used.

3.4. Comparison with experimental results

The numerical solutions for Case 1 and Case 2 described in Table 3 are compared with data obtained during the test runs. As it was already noted, the model of the gas–liquid flow through the nozzle developed by Pougatch et al. (2008) with some modifications related to the treatment of the interfacial jump condition and the turbulent drag force forms a part of the comprehensive model presented in this paper. This part has already been validated based on detailed pressure measurements along the nozzle wall. Therefore, this paper is focussing on the spray area. However for the sake of completeness some pressure data is also presented and compared with the measurement value obtained during the spraying experiments. Fig. 4 demonstrates both the simulated pressure profiles along the nozzle wall and the test values. It is evident that the agreement is very good in both the nozzle and the entrance pipe.

Next, the radial profiles of the water fluxes ($\varepsilon_l \rho_l \mathbf{V}_l \cdot \mathbf{k}$, where $\mathbf{k}$ is the vector collinear with the axis of symmetry) are compared at two different distances from the nozzle end. During the experiments, the measurements were taken across the full cross-section. However, it was observed that the circumferential variations were minimal and within the range of experimental uncertainty. Because of the axisymmetric simplification employed during modelling, the results have to be averaged along the circumferential coordinate before comparison. Fig. 5 presents the predicted and measured profiles. It can be seen that the predicted curves represent the distribution of fluxes qualitatively correct. While at 15.25 cm the flow in Case 1 exhibits a strong axial maximum and a smaller peripheral maximum, the flow in Case 2 has only one well distinguished maximum closer to the periphery. With the increase of the distance from the nozzle both cases demonstrate that the higher liquid content area shifts towards the periphery of the spray. This area of high liquid volume fraction is more pronounced for Case 2. Even though there is some disagreement between the measured points and modelling profiles, the quantitative comparison is reasonably good, especially considering the very complex nature of the modelled process and the fact that while many closure correlations were used in the model, only the critical volume fraction value was adjusted to match experimental data. It also needs to be taken into consideration that due to the measurement technique, described in Section 3.2, the experimental points are in fact the values averaged around the 1 cm diameter circle.

3.5. Influence of the phase inversion critical liquid volume fraction values

It is instructive to investigate the influence of the choice of the critical volume fraction value on the solution. We constructed two additional cases that use the same flow parameters as Case 1 (see Table 3), but different values of the critical volume fraction – 0.75 and 0.85. Next, we compare the results with the original Case 1 that uses the value of 0.8. The comparison of liquid flow rate distributions shown in Fig. 6 reveals substantial dependence of the profile on the critical volume fraction value. The reduction of the volume fraction moves the phase inversion surface upstream in the nozzle; this affects the spray shape by making it less dispersed. Alternatively, the increase of the volume fraction causes the phase inversion surface to move downstream resulting in a wider jet of liquid droplets. In addition, for the value of the volume fraction of 0.85, the axial maximum disappears, leaving only the peripheral one. The importance of the selection of the critical value of the volume fraction is substantial and further studies are indeed required. Meanwhile, the sprays resulted from gas-assisted atomization can be successfully modelled with the critical volume fraction value chosen according to the indirect experimental data.

4. Flow analysis

In order to understand the nozzle operation, the solutions for both cases are closely examined. As the flow inside the nozzle has already been investigated and described by Pougatch et al. (2008), the present analysis focuses mostly on the spray formation and dispersion; however, some features of the nozzle flow related to the atomization are also presented to facilitate understanding.

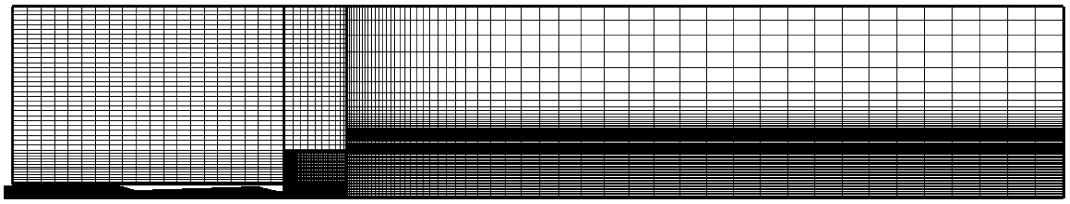

Fig. 3. Computational grid and domain segmentation.

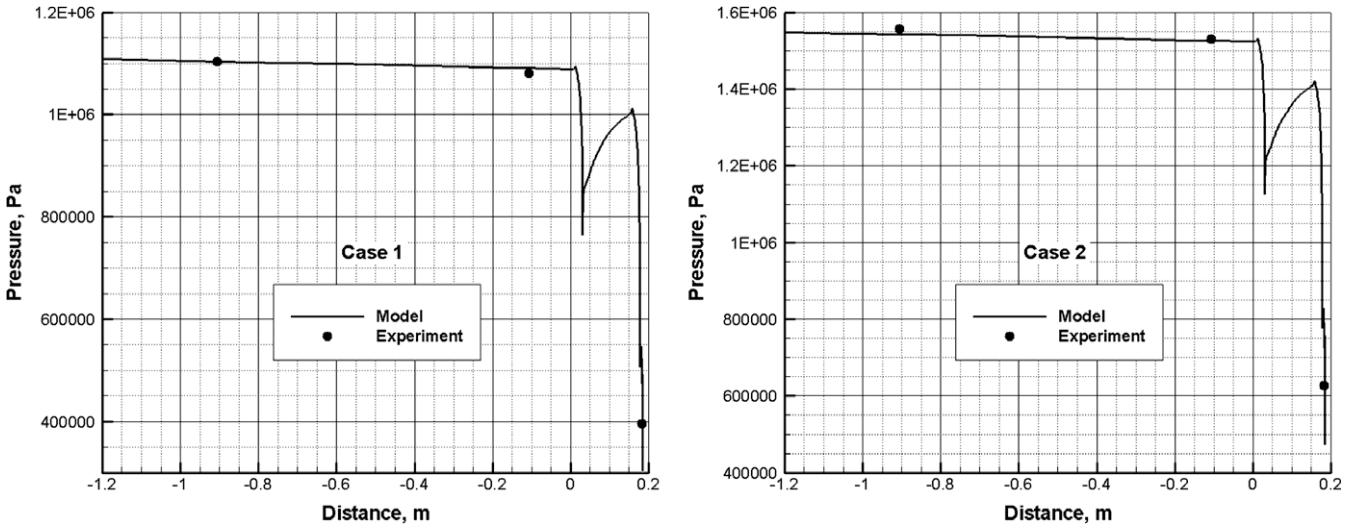

Fig. 4. Comparison between model predictions and pressure measurements along the wall of the inlet pipe and the nozzle.

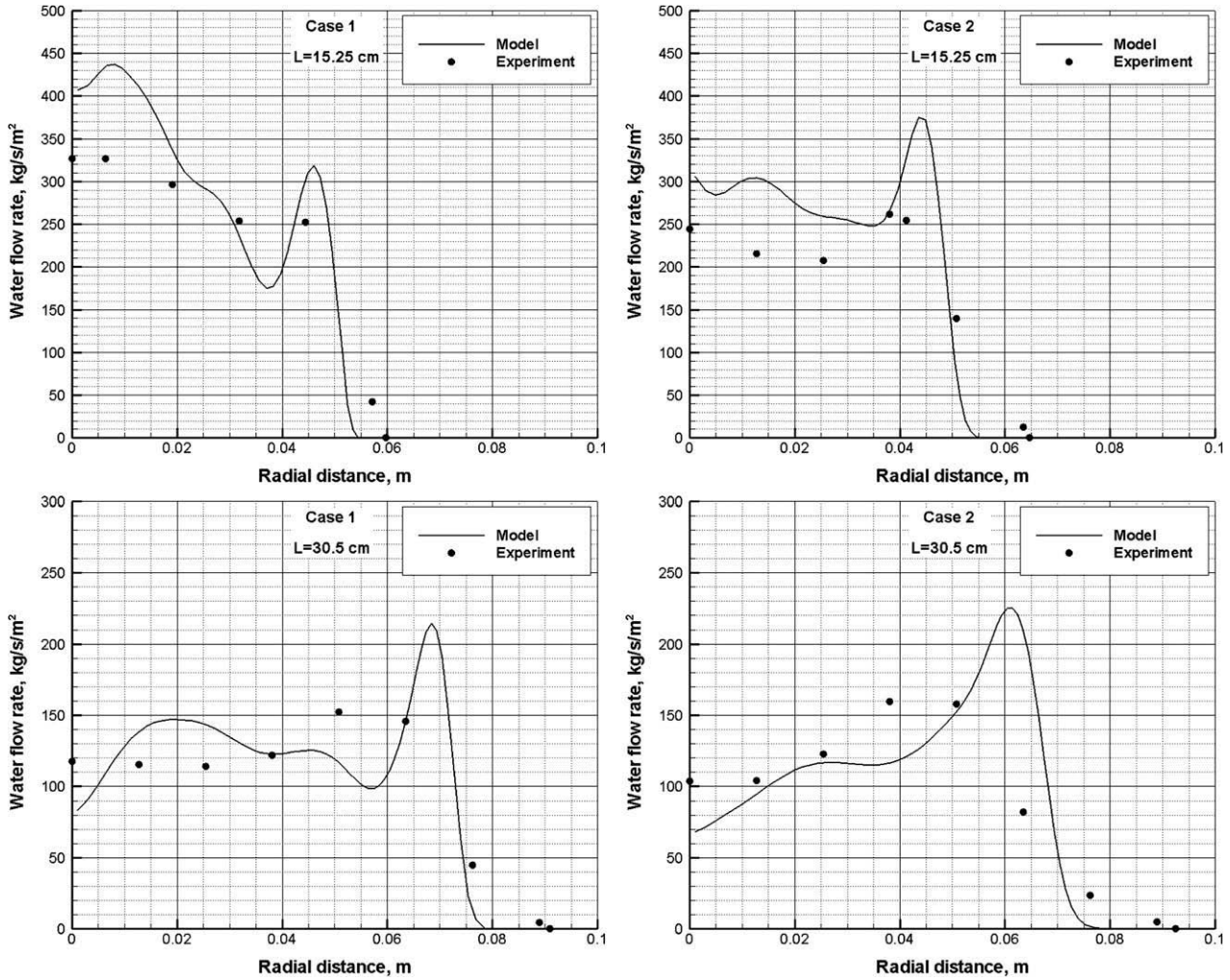

Fig. 5. Comparison between model predictions and water fluxes measurements in radial direction at different distances from the nozzle exit.

4.1. Volume fraction distribution

The contour plots of the liquid volume fractions (water, before the phase inversion surface, and droplets – after) for Case 1 are presented in Fig. 7. For viewing convenience in this and all subsequent contour plots, a cross-sectional view, which was obtained by mirroring an axisymmetric solution, is shown. The lower part of the figure shows the nozzle area, and the upper – the spray area. Note

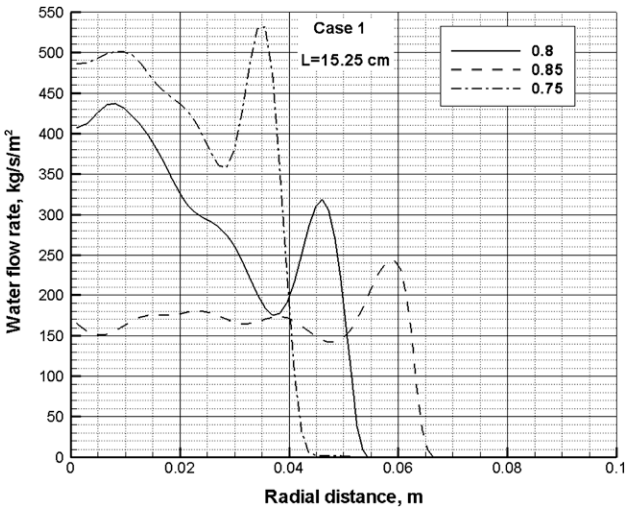

Fig. 6. Profiles of the water flow rate that correspond to the various values of the critical volume fraction.

that the scales of the colour[1] maps are different to improve presentation. It can be seen that at each convergent section of the nozzle, the phases separate due to the inertial forces. At the nozzle exit, the gradient of the volume fraction is clearly visible: there is more liquid on the periphery of the nozzle near the wall than around the centreline. According to the definition of the catastrophic phase inversion from Section 2.6 and the liquid volume fraction distribution inside the nozzle (Fig. 7), it is evident that the atomization happens near the nozzle exit plane. Thus, inside the nozzle the air is dispersed in the water as bubbles, and outside of the nozzle the droplets are dispersed in the air. The spray fills the so-called tulip shape that has been observed experimentally. This shape reflects the physics of the air-assisted atomization process under consideration. Due to the rapid pressure drop in the area around the nozzle exit (Fig. 9), the air expands, as its density decreases. Because of the interfacial forces, the drag and virtual mass for the water-continuous flow and the drag for the air-continuous flow, liquid has to be accelerated together with the gas, resulting in a more gradual pressure drop than for the pure gaseous flow. It can be seen that the areas of higher pressure extend slightly downstream the nozzle orifice. While inside the nozzle the gas acceleration is limited to the axial direction, after the exit, a significant portion of the momentum is directed radially. This radial momentum gets transferred to the droplets that begin flowing outwards; at the same time, due to continuity, the air from the outside fills in the central part of the spray. This entrained air reduces the radial momentum of the droplets; therefore, their trajectories become curved towards the axis.

It is important to note that the droplets distribution across the spray is far from being uniform. As it has been observed before in the mass flow rate profiles (Fig. 5), after a certain distance from the nozzle exit, there are more droplets in the periphery of the spray than in the centre. There are two contributing factors to this distribution. Firstly, it is connected to the non-uniformity of the phase distribution already formed before the phase inversion surface. Secondly, the influence of the air entrainment, explained above, increases with the distance from the centreline due to the larger difference between the phase velocities. Thus, the droplets in the outer part of the spray are pushed towards the centre more than the ones in the middle. It has to be noted that while plots show some discontinuity right at the centreline, which is the axis of symmetry, this is, probably, a numerical artefact of the coordinate transformations due to the axis singularity and does not have a physical meaning. The overall features of the water volume fractions distribution in the Case 2, shown in Fig. 8, are similar. However, some important differences are noticeable. The spray is visibly less dispersed and the peripheral maximum is formed at a shorter distance downstream from the nozzle than in the previous case (see also Fig. 5). The reason for such behaviour will be discussed below, after the examination of the average droplet diameter. In addition, it can be inferred from the contour plot that in the central area of the nozzle, the phase inversion takes place inside the nozzle upstream from the exit plane.

4.2. Velocity variations

Next, let us analyse the velocity distribution for both phases. Fig. 10 shows the air velocity magnitude contours for both cases. The plots demonstrate a rapid increase of the velocity right after the nozzle exit. That happens because of the significant reduction of the drag and the virtual mass forces after the atomization. Even though the air still transfers some momentum to the water droplets, this transfer is less than for the liquid-continuous flow inside the nozzle, and the gas acceleration can be higher. Downstream from the intensive expansion area, which coincides with the high pressure gradients, the air slows down due to the interfacial friction with the droplets, which in the absence of the source terms from the density decrease, becomes the dominant force in the momentum equation. As expected, comparison of the two plots for the different cases shows a substantially higher gas velocity for the higher GLR case (Case 2). The reason lies in a higher inlet air flow rate that results in a higher pressure drop, and, hence, in a higher acceleration.

As it was discussed above, the droplets are accelerated together with the air. The droplets velocity contours are presented in Fig. 11. Due to the much higher inertia of the droplets, they are slower to accelerate and slower to decelerate. Thus, even though their velocity follows the changes of the air velocity, the amplitude of the changes is less. Similarly to the air velocity, the droplets velocity

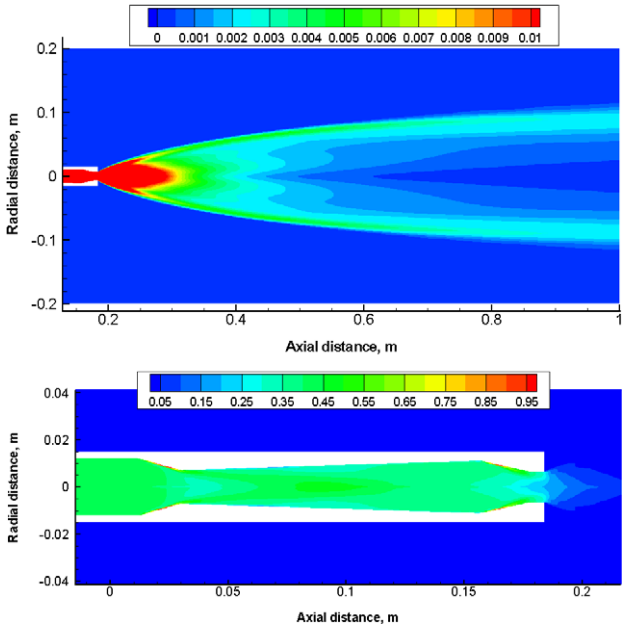

Fig. 7. Liquid volume fraction distribution in the nozzle (bottom) and in the spray (top) for Case 1 (2% GLR).

[1] For interpretation of the references to colour in Fig. 7, the reader is referred to the web version of this paper.

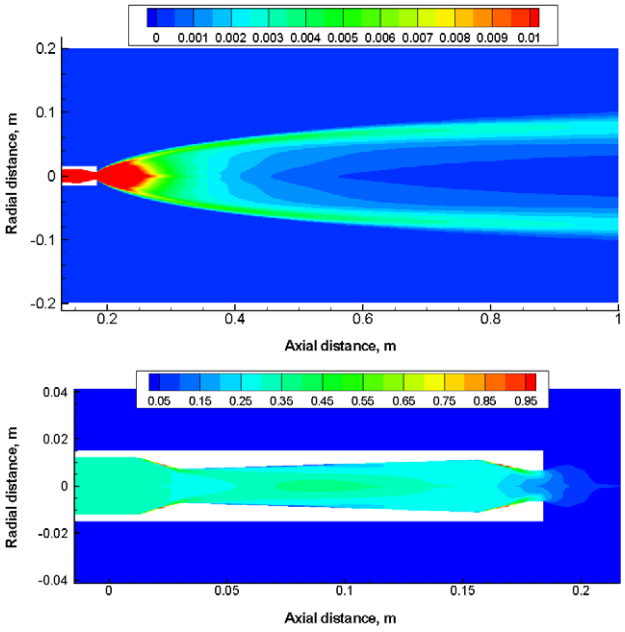

Fig. 8. Liquid volume fraction distribution in the nozzle (bottom) and in the spray (top) for Case 2 (4% GLR).

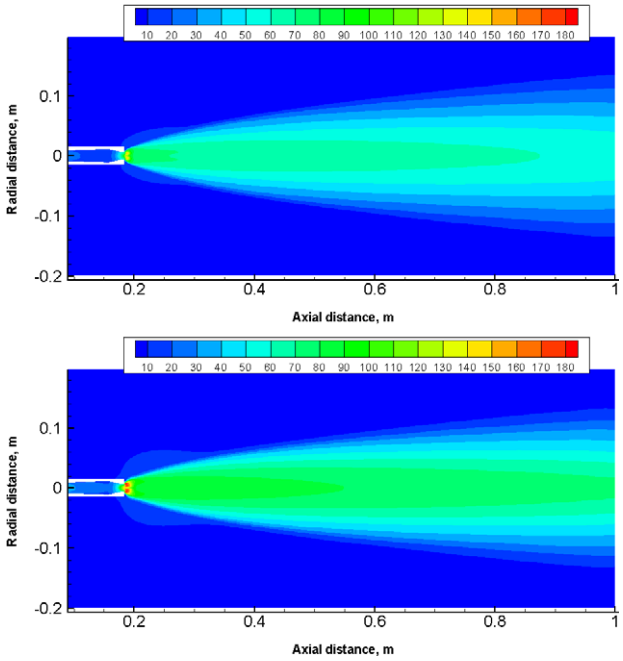

Fig. 10. Air velocity magnitude contours for Case 1 (2% GLR, top) and Case 2 (4% GLR, bottom) (in m/s).

in the Case 2 is higher than in the Case 1. It is caused by the higher air velocity and the interfacial momentum transfer.

For better understanding of the velocity variations in the spray, it is instructive to plot the phase axial velocities along the centreline on the same graph. Fig. 12 shows this graph for the two cases. It illustrates the above discussion by exposing the difference between the air and droplet velocities. It can be seen that inside the nozzle the velocity of the liquid follows closely the one of the air. Only close to the exit plane (and to the phase inversion surface) they begin to separate. Right after this plane, the air velocity spikes, causing some growth of the liquid velocity by transferring momentum to it. After the spike, the air velocity drops below the velocity of the droplets due to the higher momentum dissipation. Downstream from the points where the profiles cross, the momentum transfer is directed towards the gaseous phase keeping the air velocity from further reduction. Both velocities gradually decline, as the water jet gets dispersed. This distribution is typical for both cases; the difference is mainly in the values, which are larger for Case 2 for reasons already discussed.

4.3. Particulate phase diameter variations

Finally, let us examine the diameter of the particles. Fig. 13 presents radially averaged profiles of the average diameter of bubbles, before the atomization, and droplets, after the atomization, for both cases. In the pipe leading to the nozzle the bubble diameter

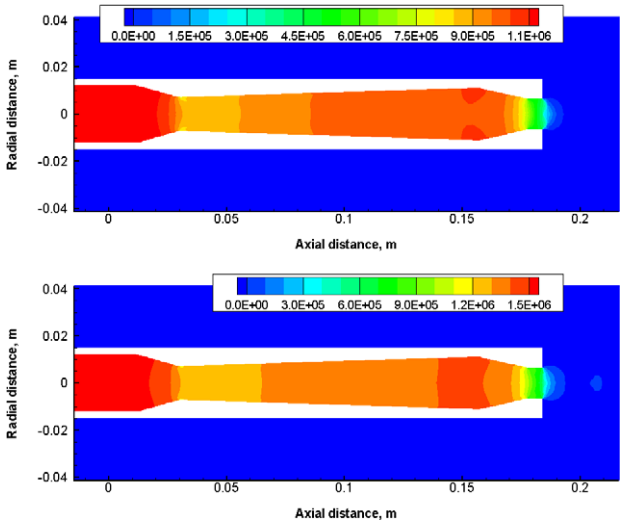

Fig. 9. Pressure contours in and around the nozzle for Case 1 (2% GLR, top) and Case 2 (4% GLR, bottom) (in Pa).

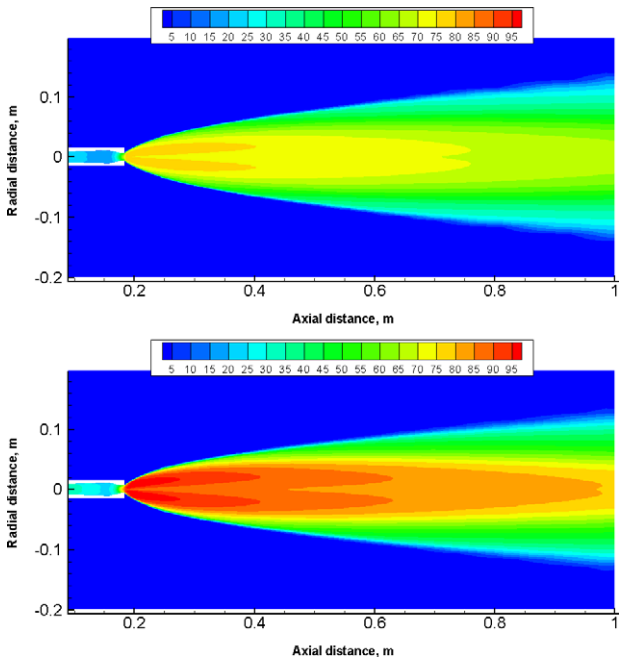

Fig. 11. Water droplets velocity magnitude contours for Case 1 (2% GLR, top) and Case 2 (4% GLR, bottom) (in m/s).

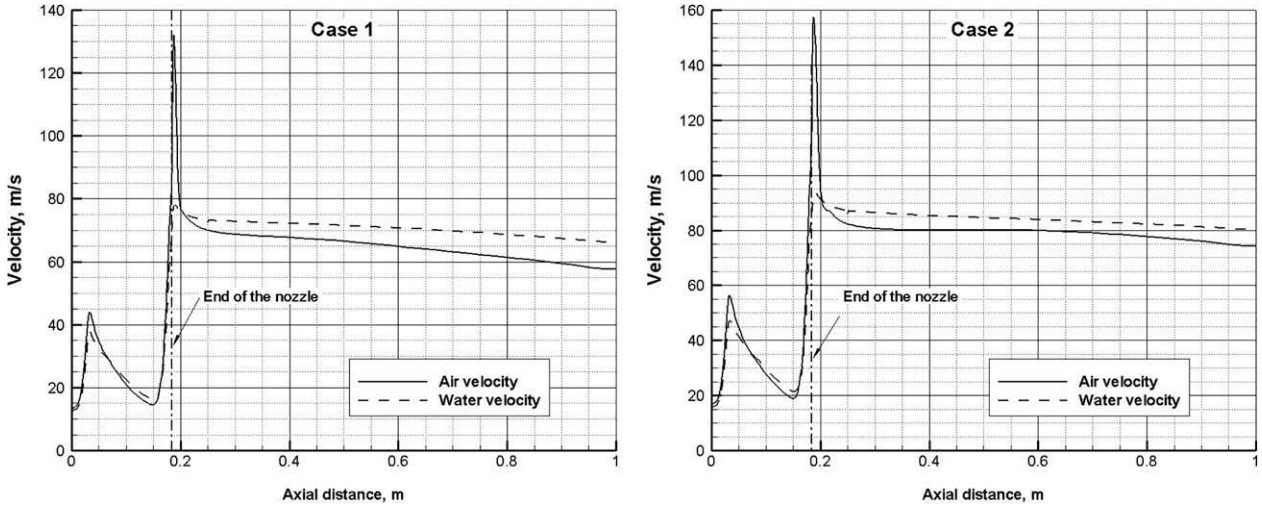

Fig. 12. Air and droplets velocity profiles along the centreline for Case 1 (2% GLR, left) and Case 2 (4% GLR, right).

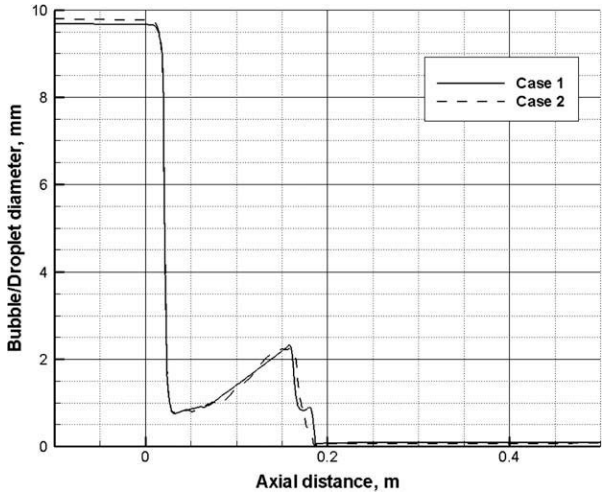

Fig. 13. Average diameter of the particulate phase (bubbles or droplets) profiles along the centreline for both cases.

is slightly less than 10 mm which is more than one-third of the pipe diameter. This value is larger than the values obtained by Pougatch et al. (2008) due to some changes in the interfacial jump and boundary conditions noted above. Inside the nozzle the bubble diameter drops below 1 mm after the first convergent section, then recovers somewhat to values around 2 mm. As the flow passes through the phase inversion surface, the diameter drops discontinuously, according to the assumptions made in Section 2.6

$$\frac{d_{droplet}}{d_{buble}} = \left(\frac{\alpha_d^{inv}}{1-\alpha_d^{inv}}\right)^{\frac{1}{3}}. \tag{73}$$

Immediately after this fall, the droplet diameter continues to decrease due to the extremely high break-up frequency. This high frequency is responsible for a relative insensitivity of the model to the prescribed values of the droplet diameter (particle number density) at the phase inversion surface. At very short distance away from the nozzle, where the rapid air expansion stops, the coalescence term begins to dominate the particle number density equation. Thus, the diameter slightly increases as the droplet flows a few centimetres away from the nozzle. It is interesting to note that for both flow regimes, liquid-continuous and gas-continuous, the

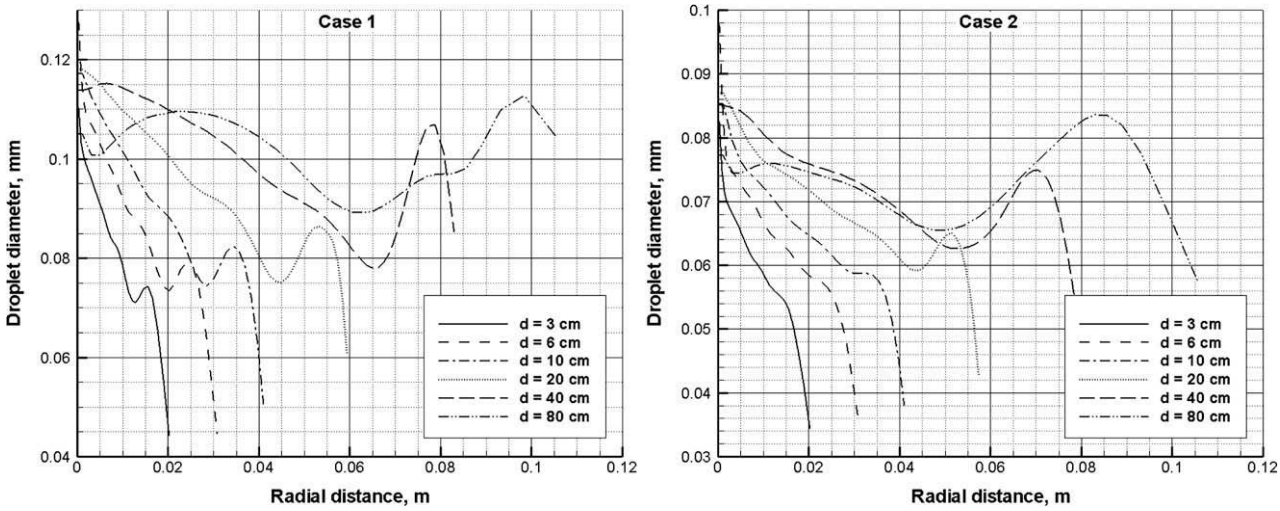

Fig. 14. Profiles of droplet diameter at different distances from the nozzle orifice for Case 1 (2% GLR, left) and Case 2 (4% GLR, right).

dominant break-up mechanism is the turbulent fluctuation of the continuous phase, as opposed to the interfacial drag. This is concluded from the analysis of the results and Eqs. (47) and (67). Even though the velocity difference is quite large directly after the atomization, the turbulent dissipation is also very large in the same area.

While inside the nozzle the bubble diameter does not exhibit substantial radial variation, outside of the nozzle the droplet diameter changes considerably in the radial direction. Fig. 14 shows radial profiles of the droplet diameter at different distances from the nozzle orifices for both cases. Generally, the largest diameter droplets are located near the centreline of the spray and the smallest – near the periphery. At the same time, a tendency can be seen for the diameter to form a second maximum closer to an outside edge of the spray. As we have already seen in Fig. 13, the droplet diameter increases slightly due to coalescence with the particle movement away from the nozzle. This growth is more significant in the vicinity of the nozzle, where the concentrations, and, hence, the coalescence rates are higher. It is clear that the droplet diameter in the Case 2 is markedly smaller than the one in the Case 1. This observation provides a key to the understanding of the difference in spray shape between the cases (Figs. 7 and 8). The smaller diameter is explained by the higher interfacial friction that the droplets are experiencing from the entrained air. Therefore, the angle of the spray expansion is smaller and the shape is less dispersed.

The range of the values of the simulated bubble diameter in the nozzle (1 mm) and droplet diameter in the spray (100 μm) corresponds to the reported experimental observations. The limited comparison with experiment does not constitute a sufficient validation, and therefore some caution is required in the interpretation of particulate phase diameter distribution.

5. Conclusions

A two-fluid Eulerian–Eulerian model with a catastrophic phase inversion has been developed for compressible gas–liquid mixtures. The model solves a single set of differential equations for the whole computational domain regardless of which phase is locally continuous. The discrete phase is assumed to be multidispersed, and the particle number density equation is solved to determine the average diameter of bubbles or droplets. The interfacial drag and the turbulence induced break-up are considered together with the coalescence of bubbles and droplets. The mixture turbulence model is adapted to liquid-continuous and gas-continuous flow regimes. As a simplified atomization treatment, an intuitive approach of modelling the phase inversion is proposed that depends on the local value of volume fractions.

The model was applied to the gas-assisted premixed atomization. The comparison of the experimentally measured and simulated values of the pressure along the nozzle wall and the water flux profiles at different distances from the nozzle orifice confirmed the capabilities of the model. It needs to be stressed that all the empirical and semi-empirical correlations used to close the model equations such as drag, virtual mass, break-up, etc., are used in their original form. The only parameter adjusted based on the experimental data is the critical value of the volume fraction which is used in the phase inversion model. Note that its range still corresponds to scarce published values. There are no other tune ups or adjustments. Even though no accurate measurements of the bubble or droplet diameter have been performed, the obtained ranges of the bubble and droplet diameter are consistent with the experimental observations.

The model application enables us to analyse the flow features and understand the reasons for the developing droplet distribution pattern. The model can be used to evaluate possible nozzle designs, investigate various operating conditions, and study the use of different liquids and gases.

Acknowledgements

The financial contribution from Natural Sciences and Engineering Research Council of Canada (NSERC) and Syncrude Canada Ltd. is gratefully acknowledged. The authors would also like to thank Darwin Kiel and Jonathan Tyler at Coanda Research and Development Corporation for many helpful discussions.

References

Batchelor, G.K., 1956. The Theory of Homogeneous Turbulence. Cambridge University Press, Cambridge.
Beck, J.C., Watkins, A.P., 2003. Simulation of water and other non-fuel sprays using a new spray model. Atomization Spray 13, 1–26.
v. Berg, E., Edelbauer, W., Alajbegovic, A., Tatschl, R., Volmajer, M., Kegl, B., Ganippa, L.C., 2005. Coupled simulations of nozzle flow, primary fuel jet breakup, and spray formation. J. Eng. Gas Turbi. Power 127, 897–908.
Behzadi, A., Issa, R.I., Rusche, H., 2004. Modelling of dispersed bubble and droplet flow at high phase fractions. Chem. Eng. Sci. 59, 759–770.
Brauer, H., 1992. Fluid flow around accelerated and decelerated particles. Waerme Stoffuebertragung 27, 93–101.
Chesters, A.K., 1991. The modeling of coalescence processes in fluid–liquid dispersions. Trans. Inst. Chem. Eng. 69, 259–270.
Deichsel, M., Winter, E.R.F., 1990. Adiabatic two-phase pipe flow of air-water mixtures under critical flow conditions. Int. J. Multiphase Flow 16, 391–406.
Deux, E., Sommerfeld, M., 2006. Modelling of turbulent atomization combining a two-fluid and a structure function approach. Atomization Spray 16, 103–125.
Drew, D.A., Passman, S.L., 1999. Theory of Multicomponent Fluids. Springer, New York.
Dukowicz, J.K., 1980. A particle–fluid numerical model for liquid sprays. J. Comput. Phys. 35, 229–253.
Gosman, A.D., Lekakou, C., Politis, S., Issa, R.I., Looney, M.K., 1992. Multidimensional modelling of turbulent two-phase flow in stirred vessels. AIChE J. 38, 1946–1956.
Hibiki, T., Ishii, M., 1999. Interfacial area transport of air-water bubbly flow in vertical round tubes. In: Proceedings of the 33rd National Heat Transfer Conference, Albuquerque, New Mexico.
Hinze, J.O., 1955. Fundamentals of the hydrodynamic mechanism of splitting in dispersion process. AIChE J. 1, 289–295.
Ishii, M., Zuber, N., 1979. Relative motion and interfacial drag coefficient in dispersed two-phase flow of bubbles, drops and particles. AIChE J. 25, 843–855.
Kataoka, I., Serizawa, A., 1989. Basic equations of turbulence in gas–liquid two-phase flow. Int. J. Multiphase Flow 15, 843–855.
Kocamustafaogullari, G., Smits, S.R., Razi, J., 1994. Maximum and mean droplet sizes in annular two-phase flow. Int. J. Heat Mass Transfer 37, 955–965.
Kolev, N.I., 2002a. Multiphase Flow Dynamics: 1. Fundamentals. Springer, Berlin.
Kolev, N.I., 2002b. Multiphase Flow Dynamics: 2. Thermal and Mechanical Interactions. Springer, Berlin.
Kolmogorov, A.N., 1949. On the disintegration of drops in a turbulent flow. Dokl. Akad. Nauk SSSR 66, 825–828.
Lasheras, J.C., Vilermaux, E., Hopfinger, E.J., 1998. Break-up and atomization of a round water jet by a high speed annual air jet. J. Fluid Mech. 357, 351–379.
Laurien, E., Niemann, J., 2004. Determination of the virtual mass coefficient for dense bubbly flows by direct numerical simulation. In: Proceedings of the 5th International Conference on Multiphase Flow, Yokohama, Japan, Paper No. 388.
Lee, C.S., Reitz, R.D., 2001. Effect of liquid properties on the breakup mechanism of high speed liquid drops. Atomization Spray 11, 1–19.
Leonard, B.P., 1979. A stable and accurate convection modelling procedure based on quadratic upstream interpolation. Comput. Meth. Appl. Mech. Eng. 19, 59–98.
Martinez-Bazan, C., Montanes, J.L., Lasheras, J.C., 1999. On the breakup of an air bubble injected into a fully developed turbulent flow. Part 1. Breakup frequency. J. Fluid Mech. 401, 157–182.
Nasr, G.G., Yule, A.J., Bendig, L., 2002. Industrial Sprays and Atomization. Springer, London.
Nijdam, J.J., Guo, B., Fletcher, D.F., Langrish, T.A.G., 2006. Lagrangian and Eulerian models for simulating turbulent dispersion and coalescence of droplets within a spray. Appl. Math. Model. 30, 1196–1211.
Pilch, M., Erdman, C.A., Reynolds, A.B., 1981. Acceleration Induced Fragmentation of Liquid Drops, Department of Nuclear Engineering, University of Virginia, Charlottesville, VA, NUREG/CR-2247.
Pougatch, K., Salcudean, M., Chan, E., Knapper, B., 2008. Modelling of compressible gas–liquid flow in a convergent–divergent nozzle. Chem. Eng. Sci. 63, 4176–4188.
Santiso, E., Muller, E.A., 2002. Dense packing of binary and polydisperse hard spheres. Mol. Phys. 100, 2461–2469.
Shi, H., Kleinstreuer, C., 2007. Simulation and analysis of high-speed droplet spray dynamics. J. Fluid Eng. 129, 621–633.
Schiller, L., Naumann, A.Z., 1935. Z. Vere. Deuts. Ing. 77, 318.

Simonin, O., He, J., 1992. Eulerian Prediction of the Particle Behaviour in a Turbulent Boundary Layer. EDF – Electricite de France, Clamart, France.
SLATEC Common Mathematical Library, 1993. Available from: <http://www.netlib.org/slatec>.
Spalding, D.B., 1980. Numerical computation of multiphase flow and heat transfer. In: Taylor, C., Morgan, K. (Eds.), Recent Advances in Numerical Methods in Fluids, vol. 1. Pineridge Press, Swansea, pp. 139–168.
Taitel, Y., Dukler, A.E., 1976. A model for predicting flow regime transitions in horizontal and near horizontal gas–liquid flow. AIChE J. 22, 47–55.
Troshko, A.A., Hassan, Y.A., 2001. A two-equation turbulence model of turbulent bubbly flows. Int. J. Multiphase Flow 27, 1965–2000.
Vaessen, G.E.J., Visschers, M., Stein, H.N., 1996. Predicting catastrophic phase inversion on the basis of droplet coalescence kinetics. Langmuir 12, 875–882.
Vallet, A., Burluka, A.A., Borghi, R., 2001. Development of a Eulerian model for the "atomization" of a liquid jet. Atomization Spray 11, 619–642.
Viollet, P.L., Simonin, O., 1994. Modelling dispersed two-phase flows: closure validation and software development. Appl. Mech. Rev. 47, S80–S84.
Wang, T., Wang, J., Jin, Y., 2005. Theoretical prediction of flow regime transition in bubble columns by the population balance model. Chem. Eng. Sci. 60, 6199–6209.
Wells, M.R., Stock, D.E., 1983. The effects of crossing trajectories on the dispersion of particles in a turbulent flow. J. Fluid Mech. 136, 31–62.
Zhang, D.Z., Prosperetti, A., 1994. Ensemble phase-averaged equations for bubbly flows. Phys. Fluids 6, 2956–2970.